


# Self-optimizing method and software for calibration and mapping of a laser system for laser machining

## Journal Article

**Author(s):**

Putzer, Matthias; Zweifel, Marc; Kneubühler, Fabian; da Silva, G. Rogério; Michael, Kiran; Schröder, Nikolai; Schudeleit, Timo; Bambach, Markus ; Wegener, Konrad

**Publication date:**

2024-07

**Permanent link:**

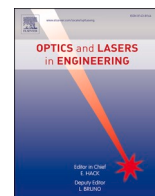
<https://doi.org/10.3929/ethz-b-000670816>

**Rights / license:**

[Creative Commons Attribution 4.0 International](#)

**Originally published in:**

Optics and Lasers in Engineering 178, <https://doi.org/10.1016/j.optlaseng.2024.108245>



# Self-optimizing method and software for calibration and mapping of a laser system for laser machining

M. Putzer<sup>a,b,c,\*</sup>, M. Zweifel<sup>a</sup>, F. Kneubühler<sup>a,b</sup>, G. Rogério da Silva<sup>b</sup>, K. Michael<sup>a</sup>, N. Schröder<sup>b</sup>, T. Schudeleit<sup>b</sup>, M. Bambach<sup>c</sup>, K. Wegener<sup>b</sup>

<sup>a</sup> Department of Mechanical Engineering, IWF, ETH Zurich, Leonhardstrasse 21, Zurich, Switzerland

<sup>b</sup> Inspire AG, Technoparkstrasse 1, Zurich, Switzerland

<sup>c</sup> Advanced Manufacturing Laboratory, ETH Zürich, 8092 Zürich, Switzerland

## ARTICLE INFO

### Keywords:

Laser ablation  
Laser micromachining  
Field distortion  
Galvanometer  
Calibration

## ABSTRACT

Short and ultrashort pulse lasers can ablate the vast majority of materials compared to other machining methods, making them the preferred tool in many niche applications. For the use in precision machining, such laser systems need to reach machining accuracy in the range of 1  $\mu\text{m}$ . Usually, a galvanometric scanner is used in such laser systems to scan the laser beam across the scan field to mark or ablate the various materials. To achieve high accuracy, the overall laser system must be calibrated. However, such calibration is time-consuming and must be monitored at regular intervals and repeated if necessary. In this paper, a method and routine are introduced for self-optimizing calibration, monitoring and recalibration of a laser system. After calibration, the maximal deviation error of the laser system is 3.9  $\mu\text{m}$  within the 30 mm x 20 mm scan field, and the optical axes are capable to match the positioning accuracy of the mechanical axes at 1.11  $\mu\text{m}$ . A beam profiling camera is used to measure the beam position needed for calibration within the scan field. At the same, time other properties of the laser beam such as peak intensity, spot size and ellipticity are mapped within the scan field and is then used as a tool fingerprint of the laser beam across the scan field. Based on this, the influence of the position-dependent beam properties on the removal rate and surface quality is determined.

## 1. Introduction

Nowadays, short, and ultra short pulse (USP) laser machining is widely used and established in processing for a wide variety of materials in numerous niche applications. Despite this fact, laser machining is a key technology for the global high-tech industry. It is used for marking plastics and ceramics for integrated circuits [1] or engine components [2], for structuring and texturing surfaces to improve electrical, biological or optical properties [3], for stripping thin electrical wires [4], for micromachining to produce high precision three dimensional shapes [5–7] or for drilling holes [8,9] and for laser cutting of printed circuit boards [10] as well as OLED displays [11] and their repair [12].

In modern laser systems for surface micromachining, a galvanometer scanner is usually used in combination with lenses to deflect the laser beam across the scan field. Often, the scan field cannot cover the full surface of a workpiece. Mechanical linear axes are used to extend the working space of the laser system to machine large workpieces. The exact positioning accuracy of an industrial galvanometer scanner with

a lens objective ( $f = 163 \text{ mm}$ ) is typically in the range of 150  $\mu\text{m}$ , according to the Scanlab GmbH product brochure [13]. For high-precision processing, the mechanical and optical axes must be aligned precisely and all distortions coming from the propagation of the laser light along its path through multiple lenses and mirrors must be compensated. Xie et al. [14] and Zhang et al. [15] gave an overview of the most often observed errors in such laser systems, with the distortion caused by the lenses used to focus the laser beam being the most significant for modern laser systems. This distortion can be determined using optical design programs such as ZEMAX. Zhimuleva et al. [16] use ZEMAX in their work to design the layout of telecentric objectives and determine the distortion over the diameter of the telecentric objective. This distortion can then be used to create calibration files for the lens objective. Manakov et al. [17] describe a model-based approach for calibrating a galvo scanner. They model the scan mirrors as ideal planes and use vector calculations to obtain the direction of the deflected laser beam from the direction of the laser beam going into the galvo scanner. Even though the model gives a good approximation of galvo scanner distortion, they

\* Corresponding author at: inspire AG, Technoparkstrasse 1, 8005 Zürich, Switzerland.

E-mail address: [matthias.putzer@inspire.ch](mailto:matthias.putzer@inspire.ch) (M. Putzer).

<https://doi.org/10.1016/j.optlaseng.2024.108245>

Received 15 November 2023; Received in revised form 25 March 2024; Accepted 14 April 2024

Available online 25 April 2024

0143-8166/© 2024 The Author(s). Published by Elsevier Ltd. This is an open access article under the CC BY license (<http://creativecommons.org/licenses/by/4.0/>).

are still restricted by their geometrical assumptions (e.g., flat mirrors, mirror rotation axis on the reflective surface) as stated by Godineau et al. [18]. Therefore, the calibration files provided by lens manufacturers or laser system manufacturers, which were created by simulation only, usually do not allow positioning accuracy in the range below 150  $\mu\text{m}$  over the entire scan field, as mentioned above.

For high precision machining in research and industry, the accuracy of the laser system must be measured on the system and meet the necessary requirements. There are different solutions for this. Delgado et al. [19] used a coaxially coupled vision device on the galvoscanner and a self-designed calibration plate. They used the laser source to illuminate markings on the calibration plate and measured the markings with a camera. A more widespread solution for calibration, is to inscribe markings onto a medium and measure their position. From this measurement the position corrections can be obtained and used for individual calibration of a laser system as described by Chen et al. [20] or Chen et al. [21]. Bessmeltsev et al. [22] achieved a maximal deviation of 4.2  $\mu\text{m}$  and 3.9  $\mu\text{m}$  in the two optical axes directions inside a 20 mm x 20 mm scan field after inscribing markings and measuring their position and compensating for them. They machined a grid of continuous lines on a polished silicon plate and measured the surface with a confocal microscope. They then used their own cross correlation algorithm to determine the positions of the markings. A different method of using computer vision to measure the marked laser positions on the writing medium was developed by Chen et al. [23]. They took an image of a laser machined grid by a camera that is mounted on the laser setup and automatically measured all the intersection positions after skeletonization of the images. After one calibration, the radial error of a circle with radius of 10 mm is reduced to  $\pm 10 \mu\text{m}$ .

To conclude it is necessary to measure and approve the final accuracy of the laser system across the scan field. The beforementioned literature has shown that marking a grid seems most suitable here. The solid lines allow for easy detection of deviations and the intersections can be used to measure the positions and subsequently calculate a calibration file. Hence, an automatic software and routine is presented in this work, for self – optimizing calibration of a laser system for micromachining. The measured deviations of a single axis (x, y, u or v) at different positions within the scan field are interpolated and described as a surface. From this, a calibration file with a higher resolution than measured can be created. For stability of the laser movement at the edges of the scan field the surface is extrapolated. It is well known that extrapolation with polynomial functions grow extremely beyond the interpolated data. Radial basis functions can technically be used for extrapolation and allow smoothing that significantly reduces the extreme growth beyond the interpolated data. Furthermore, the work of Grzhibovskis et al. [24] highlighted the use of radial basis functions on digitized surfaces and showed that different basis functions can be used without much coding effort, making them suited for optimization.

Furthermore, it is the first time with this work that a beam profiling camera is used for measurement, calibration and recalibration purposes, according to our knowledge. In addition, the beam profiling camera is used to map different beam properties across the scan field leading to a tool fingerprint of the laser system. The tool fingerprint is a newly concept within the scope of this work, and to the best of the authors knowledge, has never been presented before for laser material processing. From this, the maximal markable size of the scan field as well as the area for uniform beam properties is determined. Finally, a flat oxygen free copper plate is processed by ultra short pulse laser ablation to evaluate the influence of different beam properties on the removal rate and surface roughness. To the best of the authors knowledge, there are no known studies on the influence of the ellipticity of the beam cross section on material removal. Overall, this work highlights the importance ensuring the accuracy of the laser system and the information of the laser beam properties across the scan field to improve the processing stability and repeatability of a particular laser system.

## 2. Experimental details

### 2.1. Laser setup and material

The material chosen as medium to inscribe the markings is a precision foil made of CrNi steel 1.4310 with a thickness of 0.10 mm. It is inexpensive and easy to use, and pieces of 50 × 50 mm are cut. To increase the contrast between the lasered lines and the surrounding surface, the foil is tempered at 300 °C for 3 h which alters its color to gold brown. For the investigation of the influence of different beam properties on the removal rate and surface quality, oxygen-free copper platelets of high purity (99.95 % Cu) are used. The platelets have a thickness of 1.00 mm, a surface as obtained after rolling and are cut to pieces of 50 × 50 mm.

The laser setup calibrated in this study consist of the following components and is shown in Fig. 1. The galvoscanner used is a water-cooled intelliSCAN 14 from Scanlab GmbH with a position resolution of 20 bit ( $\sim 100 \text{ nm}$ ) and a repetition accuracy of  $< 0.4 \mu\text{rad}$  for the lateral movement of the laser spot in u- and v-direction. The laser objective is a telecentric f-theta objective S4LFT4066–292 from Sill OPTICS made of quartz glass for a wavelength of 515–545 nm with a focal length of 67.2 mm and a specified scanning range of 15 × 15 mm in combination with the stated galvo scanner. The galvoscanner, with lens is mounted on a direct drive linear stage PRO165LM from Aerotech used as the focusing axis z. For the lateral movement in x- and y-direction, two direct drive nanopositioning stages ANT180L from Aerotech Ltd. are used. The positioning accuracy and repeatability of the axis is  $\pm 150 \text{ nm}$  with a straightness and flatness error of  $\pm 1.25 \mu\text{m}$  each. The USP laser system used in this study is a Carbide from Light Conversion Ltd. with a tunable pulse duration from 190 fs – 20 ps, a center wavelength of 1030 nm and a beam quality of  $M^2 < 1.2$ . The wavelength used for this study is 515 nm green light delivered by an automatic harmonics generator fully integrated into the laser system. For the markings a pulse duration of 200 fs and a pulse repetition rate of 100 kHz at an output power of 5 W is used, the spot diameter of the laser system is 9.5  $\mu\text{m}$ . With this parameter a good contrast of the marked lines is achieved. The spot diameter is measured with the Spiricon SP620U beam profiling camera, which is equipped with a magnifying lens (10x), and after determining the optical scaling factor. This scaling factor is the ratio between the set distance and the measured distance between two mechanical axis points measured with the beam profiling camera. Fig. 1 shows schematically the setup with the three mechanical axis (x, y & a), the two corresponding optical axes (u & v) and the focusing axis z.

### 2.2. Measurement devices

The laser machined grid is measured by the optical microscope VHX – 7000 from Keyence. The microscope is in an environment with controlled temperature of  $21.0 \pm 1.0 \text{ }^\circ\text{C}$ . Prior to measurements, the Keyence microscope is calibrated using a certified calibration scale from Keyence, which has a verified accuracy of 60 nm. A 50x magnification is used for the measurements, resulting in an image resolution of 1 pixel / 2.066  $\mu\text{m}$ .

The position of the laser spot on the laser setup and its beam properties are measured in situ with a beam profiling camera. It consists of a USB silicon CCD camera (Spiricon SP620U) from Ophir and is equipped with a magnification lens (10x), a beam splitter and ND filters. The magnification lens is used to increase the size of the laser spot and the resolution of the intensity profile. The beam splitter preserves the polarization and overall intensity profile and, in conjunction with the ND filters, reduces the overall intensity of the laser beam on the sensor.

The ablated pockets for the investigation of the influence of different beam properties on the removal rate and surface quality are measured by the confocal microscope S neox (Five Axis) from Sensofar. A 20x magnification is used for the measurements.

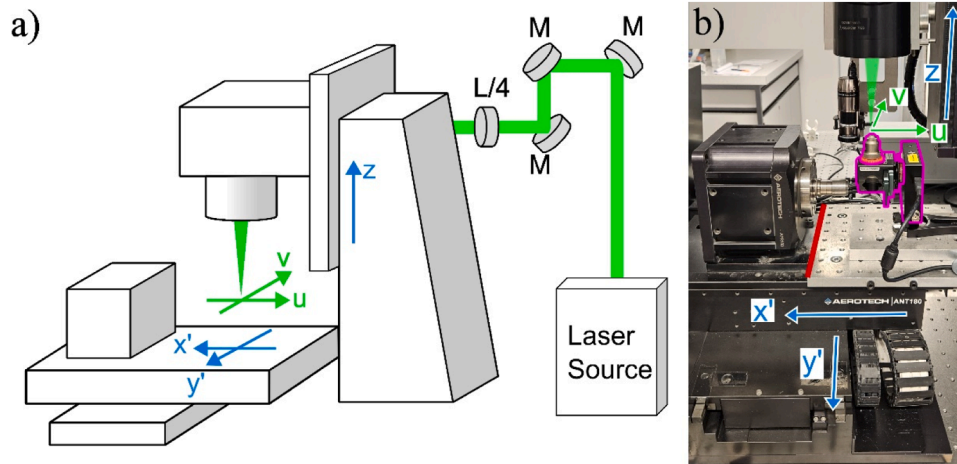


**Fig. 1.** Laser system used for the calibration. (a) shows the schematic overview of the setup and (b) is an image of the workspace. The green arrows show the laser beam with its optical axes  $u$  and  $v$ . The straight blue arrows show the linear mechanical axes  $x'$ ,  $y'$  and  $z$ . The curved blue arrow shows the rotational mechanical axis  $\alpha$ , which is part of the laser system but not used in this work. The red line shows the side length of the mounting plate, which is 20 cm x 20 cm wide.

### 2.3. Laser machining and beam movement for measurement

A grid is machined with the laser to obtain the information needed for the calibration. The laser system is preheated for 30 min to ensure a steady state. The line distance within the grid is kept constant throughout the machining process. The order in which the lines are machined is not important, and the time required for machining is small so that thermal effects do not play a role. It is important to choose the right number of lines and the right line spacing so that the scan field is covered properly and the resolution at the edges of the markable scan field is high enough. Due to automation, a large number of lines can be laser machined. The lines perpendicular to each other in the grid intersect, and these intersection points mark the real positions of the corresponding ideal positions.

After the calibration of the mechanical  $x$  and  $y$  axes and the rough calibration of the optical axes  $u$  and  $v$  is done, the beam profiling camera is mounted on the mechanical  $x$  and  $y$  axes. It is important that the maximal deviation of the optical axes  $u$  and  $v$  within the scan field are clearly smaller than the size of the CCD sensor of the beam profiling camera. This is because the deviation between the mechanical and optical axes movement is measured as a position on the CCD sensor. Then, the mechanical axes are used as masters to calibrate the galvo scanner by moving the mechanical axes  $x$  and  $y$  simultaneously with the optical axes  $u$  and  $v$  over the entire scan field and measuring the actual position of the laser spot at the corresponding ideal positions. After the final calibration of the optical axes is done, the beam properties of the laser spot are mapped by measuring them at regular positions on a dot matrix within the scan field using the beam profiling camera.

## 3. Method and software

### 3.1. Calibration – general and new concept

The general concept to calibrate a laser system for surface processing of materials, is the comparison between the ideal (commanded) and the real laser spot position (schematically shown in Fig. 2). This difference is compensated within the field of view (FoV) shown in Fig. 3. The laser spot has no physical form, and its position is determined by measuring markings (such as crosses, circles, lines etc.) or using suitable beam profiling cameras. In addition to the optical axes of the galvoscaner, most modern laser systems have also mechanical axes to move the part to increase the machinable area. The mechanical axes ( $x$  and  $y$ ) must be calibrated and aligned with the optical axes of the galvanometer scanner ( $u$  and  $v$ ) to achieve the highest accuracy to ensure a high machining

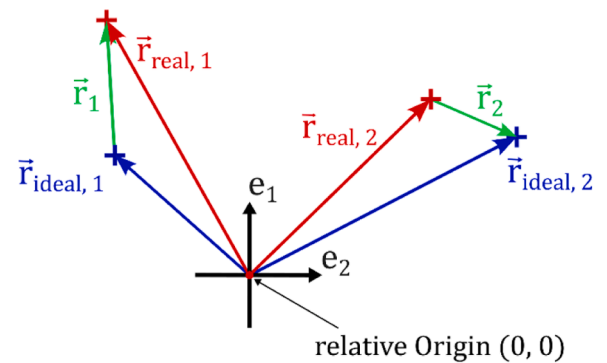


**Fig. 2.** Schematic illustration of the error vector  $\vec{r}_n$  (green) between the ideal position vector  $\vec{r}_{ideal, n}$  (blue) and the real position vector  $\vec{r}_{real, n}$  (red).

repeatability.

The calibration method proposed in this work consist of three different phases, where the flowchart of the procedure is shown in Fig. 4 and description is given in Sections 3.1 and 3.2. Each of the three phases follows the same sequence and either the sample, the tool (laser spot), or the tool together with a beam profiling camera is commanded to move to specified positions  $\vec{r}_{ideal} = (x_{ideal}, y_{ideal})$  or  $(u_{ideal}, v_{ideal})$ . At these positions  $\vec{r}_{real} = (x_{real}, y_{real})$  or  $(u_{real}, v_{real})$ , markings are made within a field of specified size and then measured by the optical microscope as  $\vec{r}_{m, meas} = (x_{meas}, y_{meas})$  or  $\vec{r}_{o, meas} = (u_{meas}, v_{meas})$  or the position of the laser spot  $\vec{r}_{o, meas} = (u_{meas}, v_{meas})$  is measured by a beam profiling camera.

In the first and second phase of the calibration process, the grid is marked on a steel precision foil and measured with the optical microscope. The intersection points between the marked lines represent the marked positions  $\vec{r}_{real} = (x_{real}, y_{real})$  or  $(u_{real}, v_{real})$ . In the first phase, the precision foil is moved by the two mechanical axes ( $x$  and  $y$ ) while keeping the laser beam constantly in the centre of the lens objective. The mechanical axes are calibrated to reach a positioning accuracy in the range of  $1 \mu\text{m}$  or subsequent calibration cycles do not further increase the accuracy. In the second phase, the laser spot is deflected by the galvanometer scanner in both optical directions ( $u$  and  $v$ ) while keeping the precision foil on the same place. Here the optical axes are calibrated to the extent that the maximal deviation of the laser spot position within the scan field is clearly smaller than the size of the CCD sensor of the beam profiling camera. This is to ensure that the measurement of the



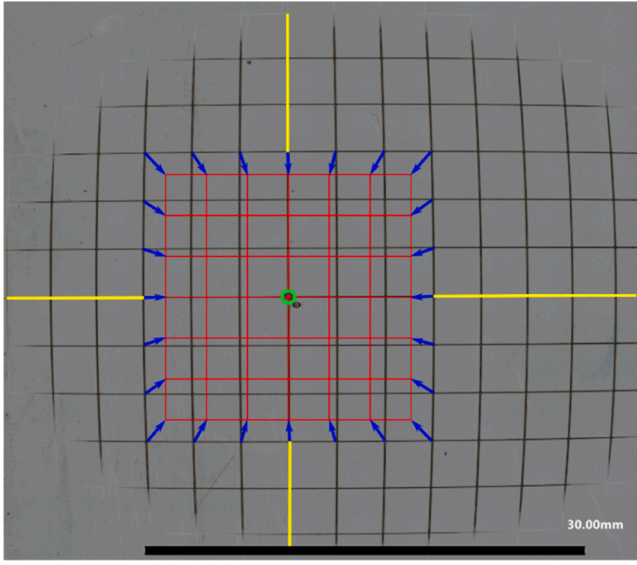


**Fig. 3.** Image of a laser marked grid (black lines) on steel (grey background) that correspond to the field of view. The green circle represents the centre of the telecentric f-theta lens, the yellow lines show the optical u and v axes. A perfect grid (goal of the calibration) is shown in red, with blue arrows pointing from the real intersection points to the ideal intersection points of the lines. The lasered grid shows a typical barrel distortion caused by the lens objective.

laser spot position in phase 3 is not hindered by the laser spot leaving the range of the CCD sensor. In the third phase, the mechanical and optical axes are commanded to move synchronously to the exact same positions.

The deviation between the mechanical and optical axes is measured on the CCD sensor after setting the center of the lens objective as origin (0, 0). The optical axes are calibrated to match the positioning accuracy of the mechanical axes in the range of 1  $\mu\text{m}$  or subsequent calibration cycles do not further increase the accuracy.

All the measurements with the microscope and the beam profiling camera are automatically analysed and processed by the software presented in Section 3.2. The measured points  $\vec{r}_{m, \text{meas}} = (x_{\text{meas}}, y_{\text{meas}})$  or  $\vec{r}_{o, \text{meas}} = (u_{\text{meas}}, v_{\text{meas}})$  are compared with the related ideal positions  $\vec{r}_{m, \text{ideal}} = (x_{\text{ideal}}, y_{\text{ideal}})$  or  $\vec{r}_{o, \text{ideal}} = (u_{\text{ideal}}, v_{\text{ideal}})$  and the deviation error,  $\Delta \vec{r}_m = (x_{\text{dev}}, y_{\text{dev}})$  for the mechanical axes and  $\Delta \vec{r}_o = (u_{\text{dev}}, v_{\text{dev}})$  for the optical axes, between them is calculated according to the following equations.

$$\Delta \vec{r}_m = \begin{pmatrix} x_{\text{dev}} \\ y_{\text{dev}} \end{pmatrix} = \vec{r}_{m, \text{meas}} - \vec{r}_{m, \text{ideal}} = \begin{pmatrix} x_{\text{meas}} \\ y_{\text{meas}} \end{pmatrix} - \begin{pmatrix} x_{\text{ideal}} \\ y_{\text{ideal}} \end{pmatrix} \quad (3.1.1)$$

$$\Delta \vec{r}_o = \begin{pmatrix} u_{\text{dev}} \\ v_{\text{dev}} \end{pmatrix} = \vec{r}_{o, \text{meas}} - \vec{r}_{o, \text{ideal}} = \begin{pmatrix} u_{\text{meas}} \\ v_{\text{meas}} \end{pmatrix} - \begin{pmatrix} u_{\text{ideal}} \\ v_{\text{ideal}} \end{pmatrix} \quad (3.1.2)$$

The two acquired deviation fields  $V_{r,xy}(x,y)$  for the mechanical axes (x and y) and the two acquired deviation fields  $V_{r,uv}(u,v)$  for the optical axes (u and v) are further refined by interpolation and the two acquired deviation fields  $V_{r,uv}(u,v)$  for the optical axes (u and v) are additionally extended by extrapolation to match the format of the calibration file. This format is predefined by the XY2 – 100 protocol of the controller for the galvo scanner and consist of  $65 \times 65$  positions divided into rows and columns. Each cell represents a specific position of the two galvanometric mirrors and for this position the correction for both optical axes is given. The interpolation of the measured intersection point is necessary to reduce the number of measurements and still obtain the required

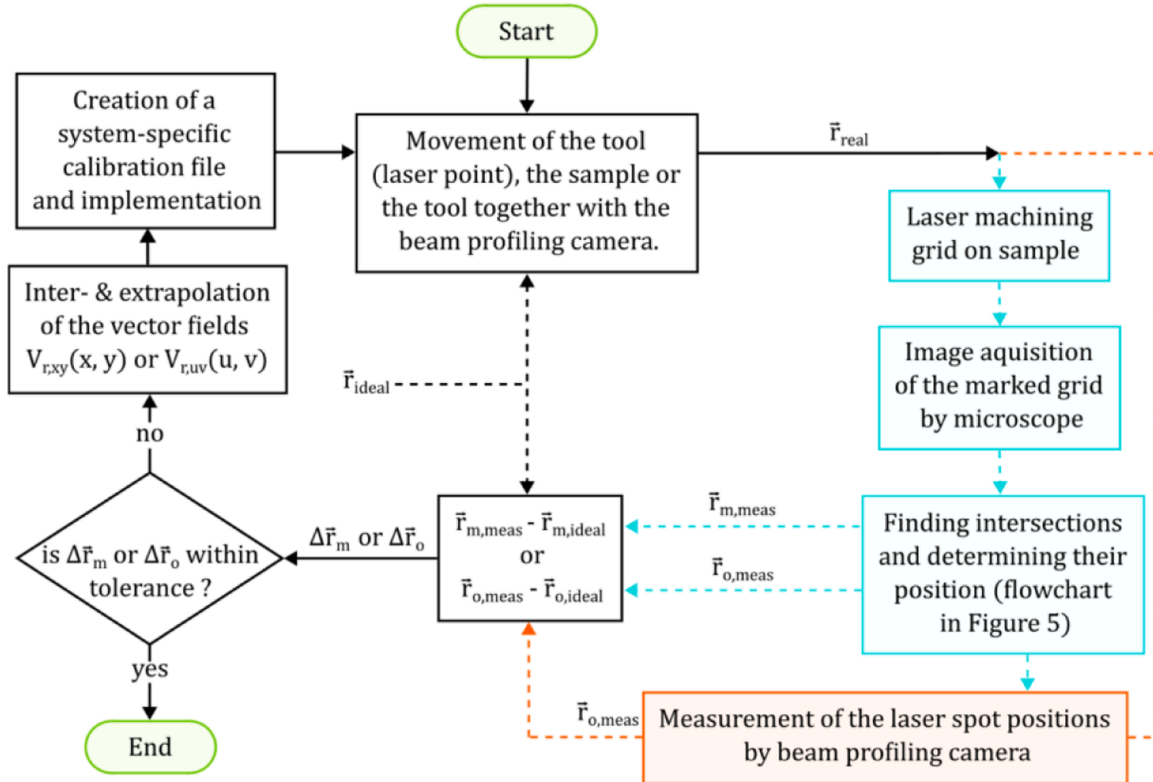


**Fig. 4.** Flowchart of the calibration process for a laser system for surface processing of materials. The calibration starts on an uncalibrated or decalibrated laser system. In the first and second phase, represented by the turquoise path, the deviations are measured on a grid marked on a flat sample (e.g., steel foil). In the third phase, represented by the orange path, the deviations are measured with a beam profiling camera (e.g., Spiricon SP620 U). The measured errors  $\Delta \vec{r}_m$  or  $\Delta \vec{r}_o$  are inter- and extrapolated to create a system specific calibration file for the laser system. After implementation of the new calibration file, the calibration process is repeated until the measured errors  $\Delta \vec{r}_m$  or  $\Delta \vec{r}_o$  are within a specified tolerance or subsequent calibration cycles do not further increase the accuracy.

number of cells. The extrapolation is necessary to avoid kinks in the motion path at the edge of the maximal markable scan field. This is because the optical axes can move the laser spot beyond the entrance of the lens objective, but it cannot be measured after the lens objective and consequently cannot be corrected. This would lead to a discontinuous calibration file, which would result in the controller having to make a jump with infinite speed. This is not physically possible but is prevented by the control system and leads to an undesirable linear interpolation between certain positions before and after the jump.

### 3.2. Software for automatic and self-optimizing calibration

The approach of this work is to fully automate the analysis and the processing of the measurements as well as automate monitoring and recalibration of the laser system. As a result, the calibration significantly speeds up and human errors are avoided. Furthermore, it provides an autonomous and self-optimizing method for monitoring, and recalibration of laser systems for material processing. The current automatic calibration software is customized to the experimental laser setup shown in Section 2. The generated calibration data, i.e. calibration file for the mechanical and optical axes, is neither encrypted nor binary. This data is returned as a matrix of the measured positions, the corresponding ideal positions, and the calculated corrections. Consequently, it can be formatted for a specific software and analysed and processed in different steps, which are shown in Fig. 5. The routine begins with a new captured microscope image of the laser marked grid that is imported into the software. For the reference within the software, the origin of the lens objective is marked with an individual marking (x-mark) on the marking medium. Then the imported image is thresholded to create a binary image that is used for further processing. First the positions of all the intersection points on the marked grid are approximated globally on the image. Then at each of the globally approximated positions an image is cut out and treated individually. This image is utilized to determine if there are two marked lines and find the centre point of their intersection. This step is repeated for all the globally approximated positions and the generated data is exported for further processing.

The illumination of the laser marked steel foil is chosen to overexpose the lasered lines, resulting in RGB values in the closer range to (255, 255, 255) in the image. Then, the microscope images are thresholded so that the lines appear white (corresponding to a greyscale value  $P_{ij} = 255$ ), and the surrounding area of the marked medium (steel foil)

appears black (corresponding to  $P_{ij} = 0$ ). This is done by checking the three colour values ( $R_{ij}$ ,  $G_{ij}$ ,  $B_{ij}$ ) of each image pixel and applying the following equation.

$$P_{ij} = 255 \cdot f(R_{ij}, t_R) \cdot f(G_{ij}, t_G) \cdot f(B_{ij}, t_B) \quad (3.2.1)$$

$$\forall x \in \{R, G, B\}, f(x_{ij}, t_x) = \begin{cases} 0, & \text{if } x_{ij} < t_x \\ 1, & \text{if } x_{ij} \geq t_x \end{cases} \quad (3.2.2)$$

Here,  $t_{\{R,G,B\}} \in [0, 255]$  are the binarization thresholds for the corresponding colour channels. In this work, the binarization threshold is set to  $t_{\{R,G,B\}} = \{245, 245, 245\}$ . The thresholded image (binary) is further processed to obtain a global approximation of the intersection points. The applied algorithm is similar to the one developed by Green et al. for line detection in images [25]. First, a horizontal rectangle next to the centre of the lasered grid (summation field) is cut out from the original image. Then, the pixels within the summation field are summed in the direction of the short side of the rectangle and subsequently normalized ( $S_{n,h}$ ), shown in Fig. 6. The same procedure is done for a vertical rectangle next to the centre of the lasered grid ( $S_{n,v}$ ). From the normalized pixel sum distributions ( $S_{n,h}$  &  $S_{n,v}$ ), all positions are extracted that overcome a threshold of 80 %. These positions are then used to create a dot grid by linear expansion of the positions to cover the whole marked area. The assumption here is that the real intersection points are in the nearby area of the approximated intersection points which are further localized in the following steps. It is important that the two centre lines of the marked grid are as parallel as possible to the corresponding image edge. The actual angle depends on the number of marked lines; the higher the number, the smaller the angle that still works. The graphical result of the global approximation of the intersection points is shown in Fig. 6.

In order to enhance the positioning accuracy of the intersection points, a square local image is extracted at each position of the approximated intersection point and checked if an intersection of two lines is found as shown in Fig. 7. For this purpose, first four rectangular fields (outlined in magenta, green, blue, cyan) next to the corresponding border (left, right, top and bottom) of the image are cut out. The length of the long side of the rectangle is equal to the border of the image and the length of the short side of the rectangle is equal to a quarter of the image length. Subsequently, the pixels within the rectangular field are summed in the direction of the short side and the obtained pixel sum distribution is normalized. From each normalized pixel sum distribution

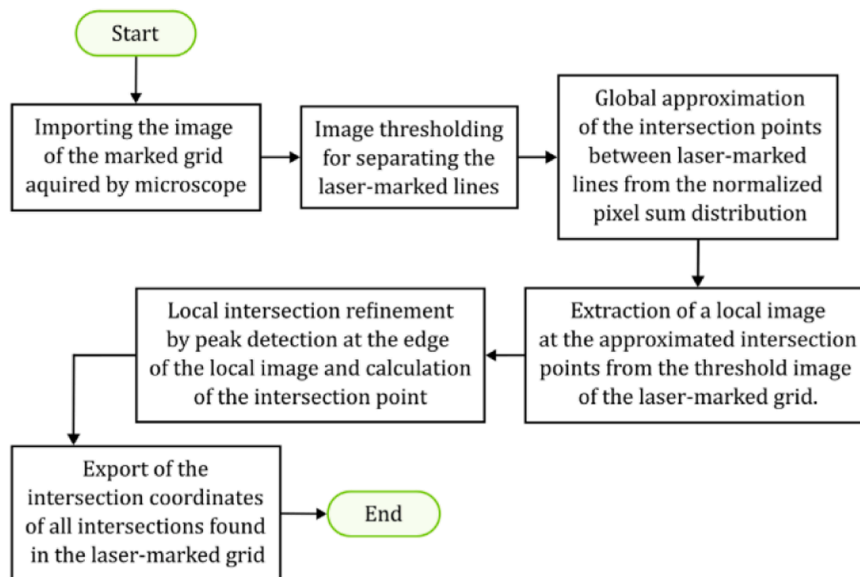


Fig. 5. Flowchart of the algorithm with different steps (programs) for the automatic analysis of the images from the microscope and for the determination of the intersection coordinates for the calibration file.

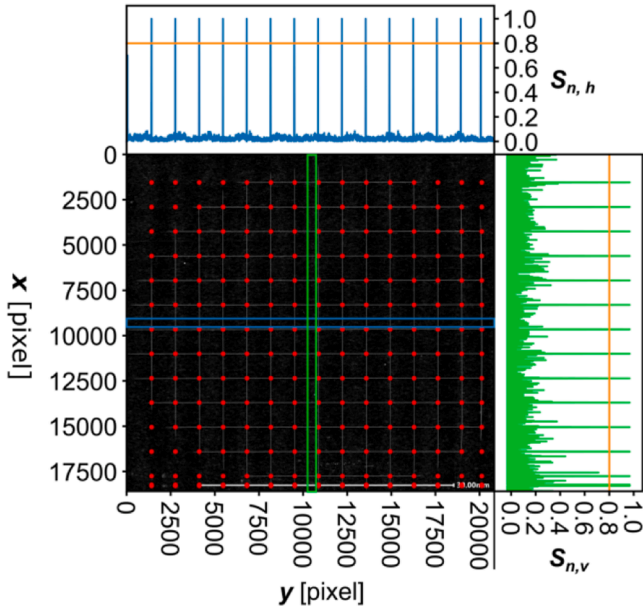


Fig. 6. Processed binary image showing the summation fields (green and blue), the normalized pixel sum distribution ( $S_{n,h}$  and  $S_{n,v}$ ) and the estimated line intersection points (red).

( $S_{n,l}$ ,  $S_{n,r}$ ,  $S_{n,t}$ ,  $S_{n,b}$ ), the position that overcomes a threshold of 60 % is extracted. This position is the intersection point of the marked line with the corresponding border (left, right, top, bottom) of the image. If four intersection points at the border are found, as shown in Fig. 7a., the intersection point of the marked lines is determined. Two opposite points represent the marked line and its direction, schematically shown in Fig. 7b. The x and y-position of the marked intersection point  $P_{x,y}$  is calculated from those two lines with the following formulae for line-line intersection.

$$P_x = \frac{(x_1 y_r - y_1 x_r)(x_b - x_t) - (x_1 - x_r)(x_b y_t - y_b x_t)}{(x_1 - x_r)(y_b - y_t) - (y_1 - y_r)(x_b - x_t)} \quad (3.2.3)$$

$$P_y = \frac{(x_1 y_r - y_1 x_r)(y_b - y_t) - (y_1 - y_r)(x_b y_t - y_b x_t)}{(x_1 - x_r)(y_b - y_t) - (y_1 - y_r)(x_b - x_t)} \quad (3.2.4)$$

In the third phase of the calibration process, a beam profiling camera is used to measure the laser spot positions (equal to intersection points) on the same grid matrix used for the calibration in phase two. The camera is mounted on a mounting plate on the mechanical x and y axis. A lens with a magnification of 10x is used to expand the size of the laser beam at the focal position, to increase the accuracy of the measurement and to capture the small laser spot of 9.5  $\mu\text{m}$ . First, a defined x- and y-axis motion within the area of calibration is executed and measured to compensate for the remaining orthogonality error, between the two mechanical axis (x and y) and the centre line of the CCD sensor, originating from the mounting of the beam profiling camera onto the mounting plate. In addition, the scaling factor between the camera sensor and the mechanical axis movement is determined. Then the mechanical and optical axes are commanded to move synchronously to the same positions on the grid matrix used for the calibration in phase two, and the deviations between the mechanical and optical axes are measured as the position of the laser spot on the CCD sensor, after the center of the lens objective is set as the origin (0,0).

Once obtained, the data from the position measurement in the first, the second or the third phase of the calibration routine is processed in the same way, as described next. The deviation of the measured positions  $\vec{r}_{m, \text{meas}} = (x_{\text{meas}}, y_{\text{meas}})$  or  $\vec{r}_{o, \text{meas}} = (u_{\text{meas}}, v_{\text{meas}})$  from the ideal position  $\vec{r}_{\text{ideal}} = (x_{\text{ideal}}, y_{\text{ideal}})$  or  $(u_{\text{ideal}}, v_{\text{ideal}})$  are calculated by Eqs. (3.1.1) and (3.1.2). Two vector fields  $V_{r,xy}(x,y)$  or  $V_{r,uv}(u,v)$  are obtained, which present the deviation from one of the two axes (x or y, u or v) at each position within the measured field of view (x,y or u,v). Lens objectives for laser systems exhibit a radially symmetric barrel distortion for which the common description is the following equation.

$$r_d(r_u) = f_1 \cdot r_u + f_2 \cdot r_u^2 + f_3 \cdot r_u^3 + f_4 \cdot r_u^4 \quad (3.2.5)$$

Where  $r_d$  is the distorted radius,  $r_u$  is the unaltered radius,  $f_1$ ,  $f_2$ ,  $f_3$  and  $f_4$  are the constants for the polynomial. The disadvantage of such a polynomial function is that it grows extremely beyond the interpolation points during extrapolation. As described in Section 3.1, the distortion (deviation field  $V_{r,o}(u,v)$ ) must be extrapolated, otherwise steps will appear in the calibration file at the edges of the field of view, causing kinks near the edge when marking. A better extrapolation approach is to

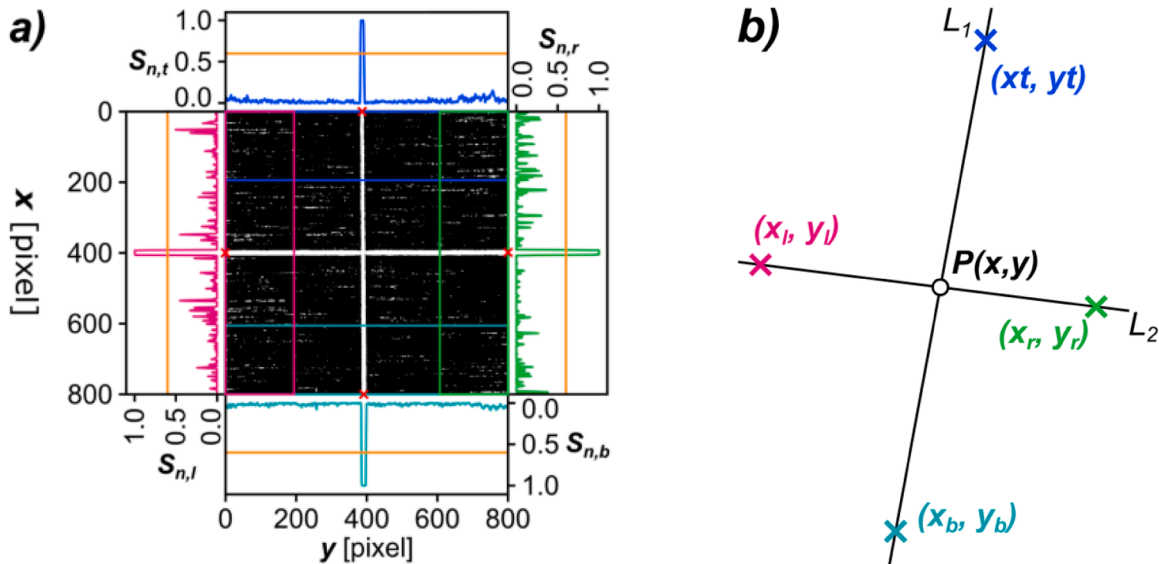


Fig. 7. a) Processed local binary image showing the summation field (blue, green, cyan, and magenta) and corresponding normalised pixel sum distribution ( $S_{n,l}$ ,  $S_{n,r}$ ,  $S_{n,t}$ ,  $S_{n,b}$ ) at each image border (top, right, bottom and left). b) Schematic representation of two intersecting lines ( $L_1$  &  $L_2$ ) defined by two distinct points  $(x_t, y_t)$ ,  $(x_b, y_b)$  and  $(x_r, y_r)$  used to determine the intersection point  $P(x,y)$ .

use radial basis functions (RBF) for interpolation, since smoothing is possible, which significantly reduces extreme growth of the extrapolation beyond the interpolation. The interpolant  $s(x)$  is expressed as the sum of radial basis functions centered at the data points in the following form.

$$s(x) = \sum_{i=1}^N a_i \Phi(\|x - x_i\|) + P_m(x) \quad (3.2.6)$$

where  $a_i$  are unknown coefficients to be determined,  $P_m$  is an  $m$ th-degree polynomial used to obtain smoothness, and  $\Phi$  is a basis function. The linear system to obtain the interpolant is solved with the module for RBF interpolation from the open-source python package (scipy). This allows for fast and easy optimization of the interpolant with respect to the chosen RBF and degree of polynomial to achieve the optimal calibration for the laser system. The inter- and extrapolated data is then utilized to create the correction file for the laser system. Most of laser scanning systems work on the XY2 – 100 protocol and the corrections are given in a matrix with signed 16-bit integer ranging from  $-32,768$  to  $32,767$ . The required size of the matrix for the laser system within this work is  $65 \times 65$  for the deviation in  $x$  and  $y$ , respectively  $u$  and  $v$  at each position.

It should also be noted that the measured deviation depends on the position of the measurement, which is not the position at which the laser is moved after correction. This is considered by introducing a measurement error  $f(\vec{r}_{\text{ideal}} + \Delta \vec{r}_{\text{corr}})$  at the position  $\vec{k} \neq \vec{r}_{\text{ideal}}$  to adjust the correction vector  $\Delta \vec{r}_{\text{corr}}$  to significantly reduce calibration cycles. This is expressed by the following formulas.

$$\vec{k} \neq \vec{r}_{\text{ideal}} \quad (3.2.7)$$

$$\vec{k} + \Delta \vec{r}_{\text{corr}} + f(\vec{r}_{\text{ideal}} + \Delta \vec{r}_{\text{corr}}) = \vec{r}_{\text{ideal}} \quad (3.2.8)$$

These conditions are fulfilled if the correct measurement error is found, which is expressed by the following constraint:

$$\Delta \vec{r}_{\text{corr}} + f(\vec{r}_{\text{ideal}} + \Delta \vec{r}_{\text{corr}}) = \vec{0} \quad (3.2.9)$$

As described above, the measured deviations for the two optical axes ( $u, v$ ) are interpolated and extrapolated using the radial base interpolant  $s_u$  and  $s_v$ , so that Eq. (3.2.9) changes as follows:

$$\begin{pmatrix} \Delta u_{\text{corr}} \\ \Delta v_{\text{corr}} \end{pmatrix} + \begin{pmatrix} s_u(u_{\text{ideal}} + u_{\text{corr}}, v_{\text{ideal}} + v_{\text{corr}}) \\ s_v(u_{\text{ideal}} + u_{\text{corr}}, v_{\text{ideal}} + v_{\text{corr}}) \end{pmatrix} = \begin{pmatrix} 0 \\ 0 \end{pmatrix} \quad (3.2.10)$$

The software created within the scope of this work is free to access and available free of charge on GitHub [26,27].

### 3.3. Mapping of the tool fingerprint

After the last calibration in the third phase is completed and the desired tolerance is achieved, the tool fingerprint of the laser system is determined. The tool fingerprint graphically represents some of the key properties of the laser tool within the field of view constraining the largest possible scan field. This is a mapping of the positioning accuracy of the laser spot, the laser spot size, the peak intensity and the ellipticity over the field of view of the galvanometer scanner. The measurement of the laser spot and its properties are done fully automatized at a high resolution as described in Section 2.3.

### 3.4. Sensitivity analysis of the calibration

After the system has been calibrated, the stability of the calibration can be monitored and corrected if necessary. For this monitoring a measurement routine is presented that is executed each time when the laser system is started and warmed up. The beam profiling camera is used to determine the position of the laser spot. The measurement

routine consists of two parts and starts in the origin of the laser system. First, a measurement circle is defined that has a diameter equal to about half of the shorter side of the beam profile camera's sensor. Then, in the first part of the measurement routine, evenly distributed positions on the circumference of this measurement circle are approached using only the movement of the optical axes and then the laser spot position is measured. The second part consists of the synchronous movement of the optical and mechanical axes to a new center position within the calibrated scan field. As shown in Fig. 8, five different centers are set for a measurement circle for the measurement routine. This determines the accuracy of the positioning of both the optical and mechanical axes within the field of view. If the accuracy of one of the axes is out of tolerance the corresponding phase of the calibration process is started to recalibrate the laser system.

## 4. Results and discussion

### 4.1. Accuracy of the calibration (phase 1) of the mechanical axes by laser marking

The accuracy of the measurements by laser marking in Sections 4.1 and 4.2 corresponds to the accuracy of the Keyence microscope used for the measurement, as described in Section 2.2. Before calibration of the positioning accuracy of the mechanical axes is measured on the as-built system described in Section 2.1 at the origin of the lens objective ( $u = 0, v = 0$ ). The initial area of calibration on the precision foil is selected with a width of  $40 \text{ mm} \times 40 \text{ mm}$  to cover the entire markable field of the uncalibrated optical axes. Figs. 9 and 10 illustrates the deviation in  $x$  and  $y$ -direction depending on  $x$  and  $y$ -position with this field. While the measured deviation error in  $x$ -direction ( $\Delta x$ ) lays between  $+61.02 \mu\text{m}$  and  $-62.62 \mu\text{m}$ , the measured deviation error in  $y$ -direction ( $\Delta y$ ) ranged from  $+12.03 \mu\text{m}$  to  $-8.74 \mu\text{m}$ . The 3D representation of the deviation error in  $x$ - or  $y$ -direction within the  $40 \text{ mm} \times 40 \text{ mm}$  field shows that this error results from an orthogonality error between the  $x$  and  $y$  axes. The error is related to assembly tolerances of the mechanical axes and/or alignment errors of the laser system that occur during assembly or disassembly for experimental work or the production of parts.

The maximal deviation error vector length ( $l_{e,xy}$ ) is used as an accuracy measure for the calibration within this work and is calculated with the following formula.

$$l_{e,xy} = \max\|\Delta \vec{r}_{xy}\| = \max\sqrt{\Delta x^2 + \Delta y^2} \quad (4.1.1)$$

This vector represents the radius of a circle which is big enough to contain all measured error vectors for all measured positions of laser markings, schematically shown in Fig. 11.

$l_{e,xy}$  for the mechanical axes of the uncalibrated laser system is  $62.8$

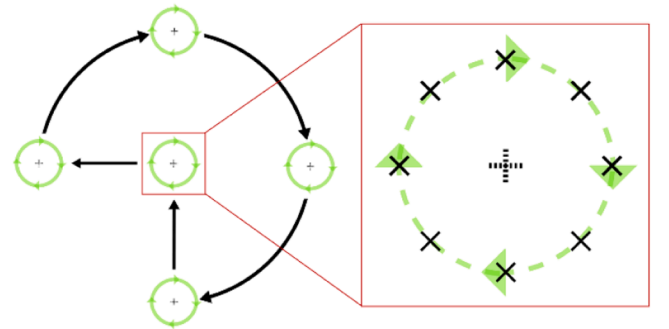


Fig. 8. Schematic representation of the measurement routine to monitor the stability of the accuracy of the laser system. The measurement starts in the origin of the laser system. For each measurement circle (green) uniformly distributed positions on the circumference (black x markings) are measured. Then, the optical and mechanical axes are moved synchronous to a new centre position of the measurement circle.



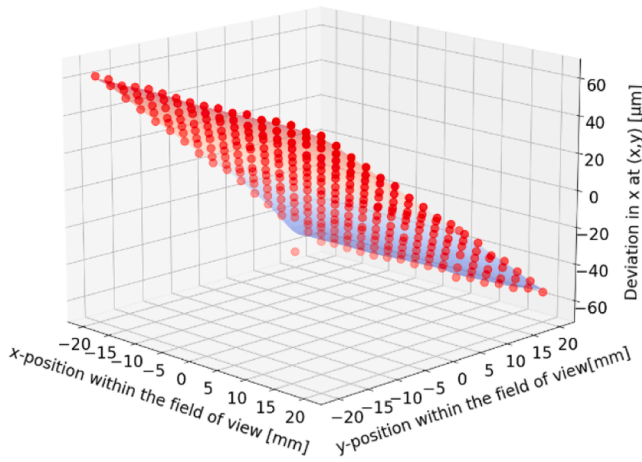


Fig. 9. 3D representation of the measured deviation in x [μm] at the position (x, y) [mm] (red circles) within the field of view of the size 40 mm x 40 mm. The measured system is uncalibrated.

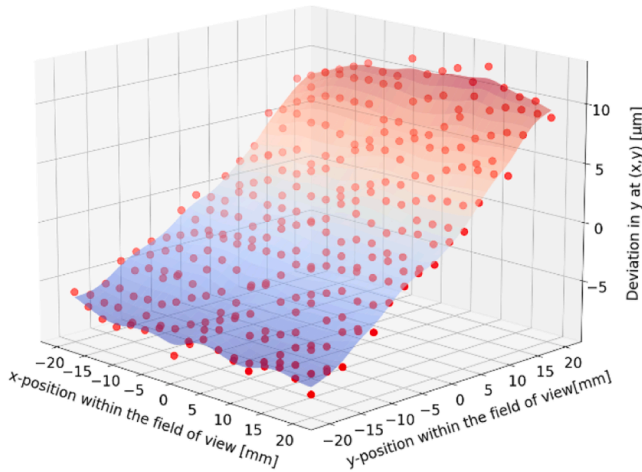


Fig. 10. 3D representation of the measured deviation in y [μm] at the position (x, y) [mm] (red circles) within the field of view of the size 40 mm x 40 mm. The measured system is uncalibrated.

μm within the 40 mm x 40 mm scan field. After the calibration iteration within phase one (procedure described in Sections 3.1 and 3.2) the measured deviation error Δx is between + 2.5 μm and - 3.5 μm. The measured deviation error Δy is between + 2.0 μm and - 3.6 μm.  $l_{e,xy}$  of the mechanical axes after calibration is 3.4 μm within the markable field. The deviation in x and y-direction as a dependency of the x and y-

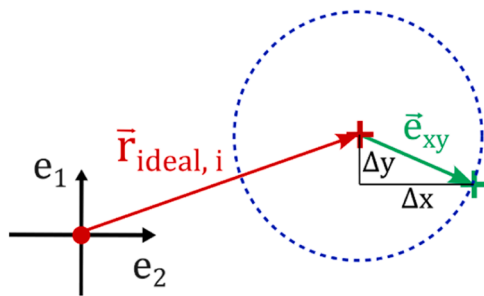


Fig. 11. Schematic representation of an ideal position (red cross) and the measured position (green cross) with the maximal deviation error vector  $\vec{e}_{xy}$ . The blue dashed circle represents the area in which all the measured deviation vectors lay.

position within the field of view is presented in Figs. 14 and 12. From the 3D representation of the deviation error in Δx or Δy, it is visible that there is no systematicity recognizable anymore.

#### 4.2. Accuracy of the calibration (phase two) of the optical axes by laser marking

Without any calibration, the movement of the galvo axes leads to curved markings due to the barrel distortion caused by the lens objective (as it can be seen in Fig. 13) and superimposed errors coming from other optical elements along the beam path. By marking a grid with the optical axis without a calibration file, the true centre of the lens objective can be determined. Two lines within the grid have no curvature and are only distorted in their direction. The intersection of these two lines is the centre of the lens objective, which is further used as origin for all subsequent calibration cycles within this work. The surface of the inter- and extrapolated deviation field, shown as an example for some basis functions  $\Phi$  in Fig. 17 for the optical axis v, is used to evaluate the function type selected for the basis function  $\Phi$  in Eq. 5. As seen in Fig. 17 The Gaussian function drops to a value of 0 beyond the interpolation data and is not suitable. The cubic and quintic functions lead to decreasing values beyond the interpolation data, which contradicts the fact that the deviation increases at the edges of the lens. The thin spline function is more sensitive to outliers, which results in the curvature of the data being lost. The linear function is less suitable for modelling complicated functions and relationships. Overall, the multiquadric function has the fewest of the limitations described above and is preferred over the others. The smoothing parameter is set to 2, which corresponds to a 2nd degree polynomial in the interpolant  $s(x)$  in Eq. (3.2.5). Although this means that the interpolant does not fit the measured values perfectly, it is less sensitive to measurement errors or errors in the image processing.

The size and shape of the calibration area in phase 2 is limited by the distortion of the laser spot at the edges of the field of view, which results in ablation ceasing and no measurable marks being produced. The measured deviation error in u-direction (Δu) within the uncalibrated field of view lays between + 2.44 mm and - 2.39 mm. The measured deviation error in v-direction (Δv) within the uncalibrated field of view lays between + 2.25 mm and - 2.24 mm. The maximal deviation error length ( $l_{e,uv}$ ) for the optical axes of the uncalibrated laser system is 2.44 mm within the field of view. From the 3D representation of the deviation error in u- or v-direction within the field of view, shown in Figs. 15 and 16, the strong symmetry coming from the barrel distortion is visible. The plotted surface corresponds to the interpolated and extrapolated data (see Section 3.2) required to cover the entire 65x65 correction matrix

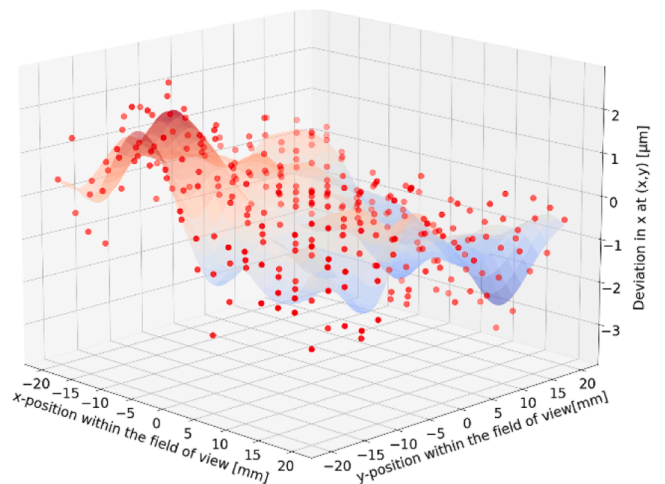


Fig. 12. 3D representation of the deviation in x [μm] at the position (x, y) [mm] within a 40 mm x 40 mm field. The deviation is measured after 1 calibration iteration of phase 1.



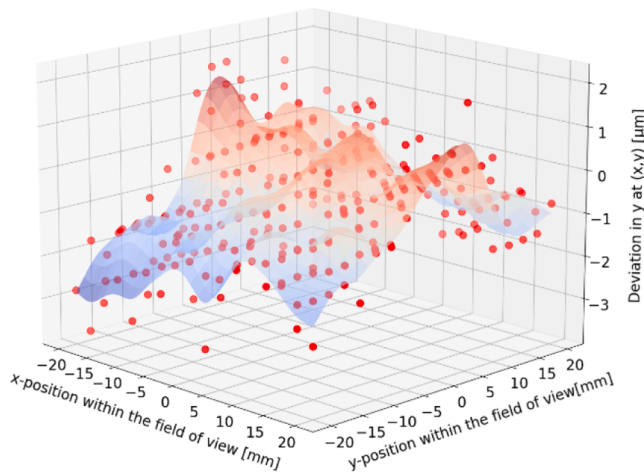


Fig. 13. 3D representation of the deviation in  $y$  [ $\mu\text{m}$ ] at the position  $(x, y)$  [mm] within a 40 mm x 40 mm field. The deviation is measured after 1 calibration iteration of phase 1.

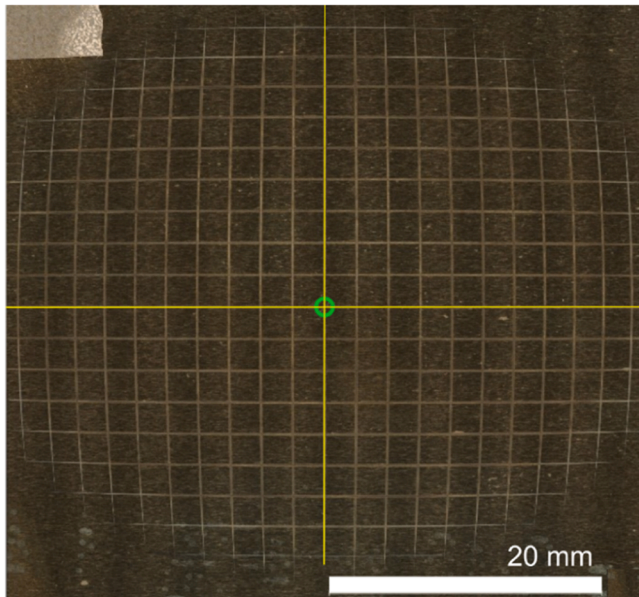


Fig. 14. Image of a laser marked grid (brown lines) on steel precision foil (grey background). The green circle represents the centre of the telecentric f-theta lens, and the yellow lines show the optical  $u$  and  $v$  axes.

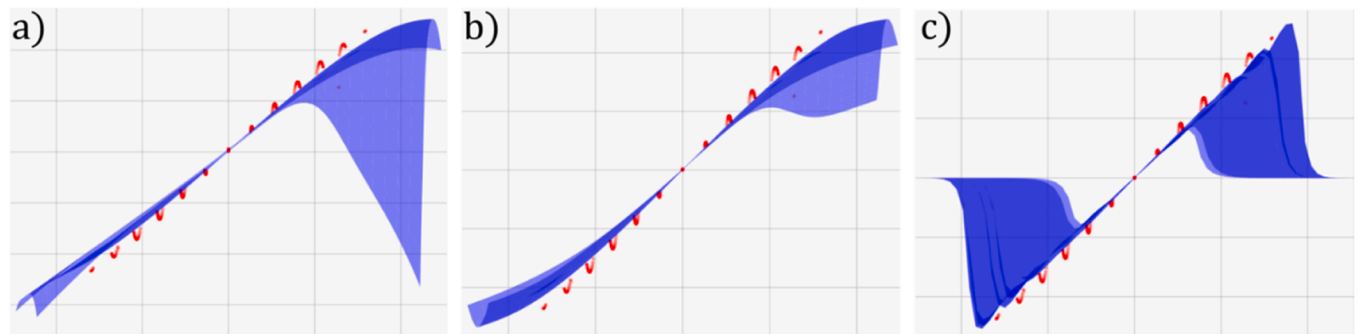


Fig. 15. Sideview of the representation of the deviation in  $v$  [mm] at the position  $(u,v)$  [mm] within the field of view from Fig. 17 to evaluate the function type selected for the radial basis function. The red dots are measurement points, and the blue surface is the interpolated data. In a) cubic basis function is used, in b) a multiquadric basis function is used and in c) a gaussian basis function is used.

for the XY2 - 100 protocol.

After one calibration in phase 2 (procedure described in Sections 3.1 and 3.2), the measured deviation error  $\Delta u$  within the field of view lays between  $+ 29.1 \mu\text{m}$  and  $- 17.7 \mu\text{m}$ . The measured deviation error  $\Delta v$  within the field of view ranged between  $+ 11.6 \mu\text{m}$  and  $- 26.8 \mu\text{m}$ .  $l_{e,uv}$  of the optical axes after one calibration in phase 2 is  $30.8 \mu\text{m}$  within the field of view. This  $l_{e,uv}$  of the laser spot position is already more than 10 times smaller than the size of the sensor of the beam profiling camera used to measure the laser spot position (deviation between mechanical and optical axes as described in Section 3.1 and 3.2) for the calibration in phase 3. After the second calibration iteration in phase 2, the positioning accuracy is further improved. The deviation error  $\Delta u$  within the field of view lays between  $+ 7.0 \mu\text{m}$  and  $- 3.8 \mu\text{m}$ . The measured deviation error  $\Delta v$  within the field of view ranges between  $+ 9.1 \mu\text{m}$  and  $- 15.3 \mu\text{m}$ .  $l_{e,uv}$  of the optical axes after two calibrations in phase 2 is  $15.73 \mu\text{m}$  within the field of view. From the 3D representation of the deviation error in  $u$ - or  $v$ -direction within the field of view (shown in Figs. 19 and 18), the distinct symmetry from the barrel distortion is not present anymore.

#### 4.3. Accuracy of the calibration (phase 3) of the optical axes by laser spot measurement

For the third phase of the calibration process, the field of view is reduced to a rectangle of size 30 mm x 20 mm with the origin at  $(0|0)$  of the origin of the lens objective. This reduction is done to take into account the increasing distortion of the beam shape towards the edges of

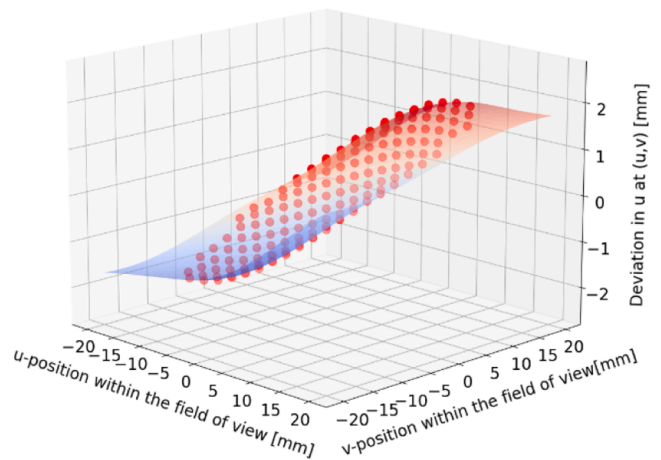


Fig. 16. 3D representation of the deviation in  $u$  [mm] at the position  $(u, v)$  [mm] within the field of view. The deviation is measured before calibrating the optical axes.

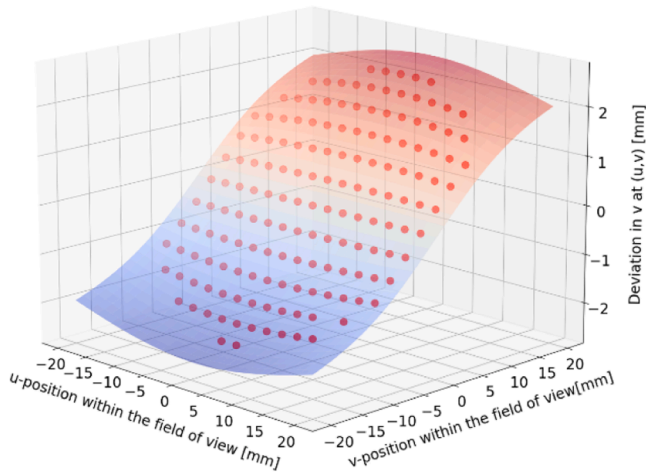


Fig. 17. 3D representation of the deviation in  $v$  [mm] at the position  $(u, v)$  [mm] within the field of view. The deviation is measured before calibrating the optical axes..

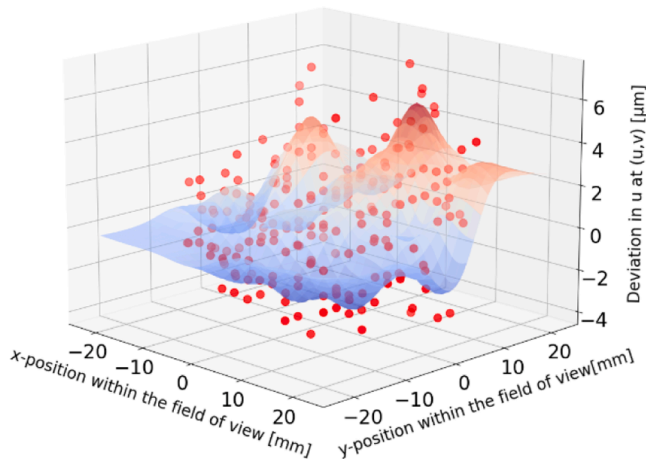


Fig. 18. 3D representation of the deviation in  $u$  [ $\mu\text{m}$ ] at the position  $(u, v)$  [mm] within the field of view. The deviation is measured after two calibration iteration of phase 2.

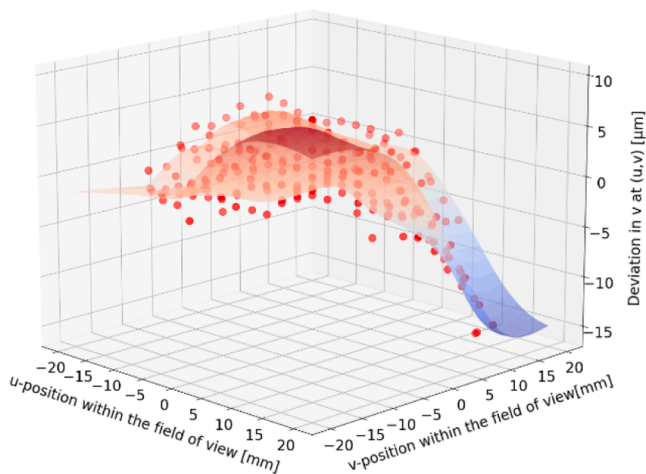


Fig. 19. 3D representation of the deviation in  $v$  [ $\mu\text{m}$ ] at the position  $(u, v)$  [mm] within the field of view. The deviation is measured after two calibration iteration of phase 2.

the lens objective, which falsifies the laser spot position measurement with the beam profiling camera. In addition, the smoothing parameter is set to 0, so that the interpolant  $s(x)$  in Eq. (3.2.5) perfectly matches the measured values and can better capture stronger oscillations between the measured positions to make a more precise correction of the deviations.

After the third calibration iteration of phase 3 (procedure described in Sections 3.1 and 3.2, the measured deviation error  $\Delta u$  within the field of view lays between  $+0.9 \mu\text{m}$  and  $-0.7 \mu\text{m}$ . The measured deviation error  $\Delta v$  within the field of view is between  $+0.9 \mu\text{m}$  and  $-1.0 \mu\text{m}$ .  $l_{e,uv}$  of the optical axes after three calibration iterations in phase 3 is  $1.1 \mu\text{m}$ . From the 3D representation of the deviation error  $\Delta u$  or  $\Delta v$  within the  $30 \text{ mm} \times 20 \text{ mm}$  field, shown in Figs. 20 and 21, it is visible that there is no systematicity recognizable. Moreover, the deviation errors appear to be random or chaotic. The maximal deviation error length of the whole laser system within the  $30 \text{ mm} \times 20 \text{ mm}$  field is  $3.9 \mu\text{m}$ . This deviation error is composed of the deviation error of the optical and mechanical axes since the mechanical axes are used to measure the optical axes.

#### 4.4. Mappings of laser beam properties within the field of view

After the mechanical and optical axes are calibrated to a final accuracy of  $3.9 \mu\text{m}$  ( $l_{e,uv}$ ), the laser beam properties are measured within the  $30 \text{ mm} \times 20 \text{ mm}$  scan field. A total of  $114 \times 76$  measurement points in  $u$ - and  $v$ -direction with an increment of  $263 \mu\text{m}$  is selected and at each position the relative intensity of the gaussian profile, the ellipticity as well as the spot diameter of the laser is measured with the beam profiling camera. The specified scan area for laser processing in the lens data sheet is specified as  $15 \text{ mm} \times 15 \text{ mm}$  for a 2-mirror system.

The relative peak intensity refers to the maximal global peak intensity measured in the entire  $30 \text{ mm} \times 20 \text{ mm}$  field. The change in relative peak intensity with varying average laser power is negligible, as the laser has an almost constant beam output diameter after the laser device. In addition, the peak intensity correlates with the fluence and can be measured without a calibration of the signal to energy ratio of the beam profiling camera. The peak intensity can be used in relative comparison to obtain information about the material removal. However, material removal is also influenced by many other factors. The mapping of the relative peak intensity, as shown in Fig. 22, illustrates an elliptical distribution that is not centred in the origin of the lens objective. The relative peak intensity decreases as moving away from the centre, dropping to approx. 50 % at the edges and corners.

It is often pointed out in the laser literature that a gaussian shaped laser spot should be as circular as possible for high precision machining,

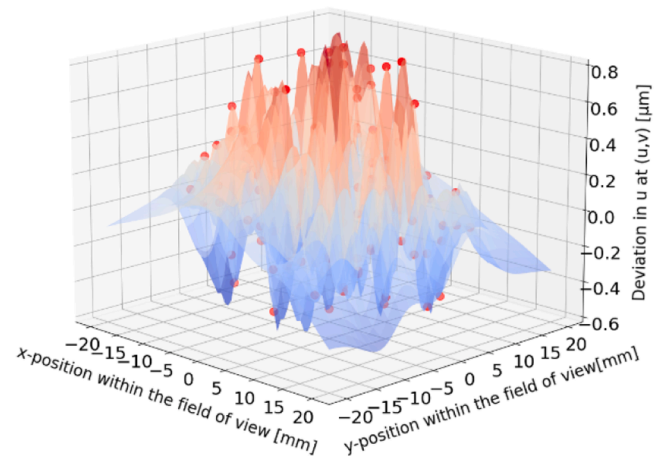


Fig. 20. 3D representation of the deviation in  $u$  [ $\mu\text{m}$ ] at the position  $(u, v)$  [mm] within the field of view. The deviation was measured after three calibration iteration of phase 3.

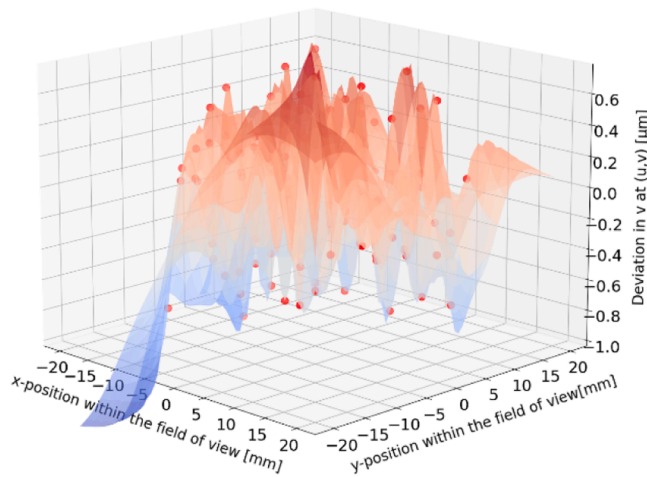


Fig. 21. 3D representation of the deviation in  $v$  [ $\mu\text{m}$ ] at the position  $(u, v)$  [mm] within the field of view. The deviation was measured after two calibration iteration of phase 3.

as the fluence is then distributed most evenly over the focal spot. With flat field lenses the laser beam has different angles of incidence at each position within the focal plane, which leads to increased elliptical beam shape towards the edges of the field of view leading to changes in the material removal and surface quality. For this reason, telecentric f-theta lenses are used for high accuracy precision machining. The mapping of the ellipticity, shown in Fig. 23, within the field of view shows that the beam spot is not circular throughout the field of view for this telecentric f-theta lens. In addition, the distribution is not centred in the origin of the lens objective.

According to DIN EN ISO 11146-1 [28] a beam can be considered circular if the ellipticity ( $\epsilon$ ) is greater than 0.87. The ellipticity  $\epsilon$  is calculated from the ratio of the major ( $d_{\sigma M}$ ) and minor ( $d_{\sigma m}$ ) axis of the intensity distribution of the gaussian laser beam, as shown in Fig. 25, according to the following equation.

$$\epsilon = \frac{d_{\sigma m}}{d_{\sigma M}} \quad (4.3.1)$$

The area within the scan field where the beam is circular is shown by the red contour lines in Fig. 23. Outside of it the beam shape is elliptical. For this reason, a better overall representation of the beam shape and dimension is given from the two mappings, shown in Figs. 24 and 26. The  $d_{\sigma M}$  changes more significantly across the mapped field than  $d_{\sigma m}$ . Nevertheless, the change of the beam shape is significantly. It is nearly

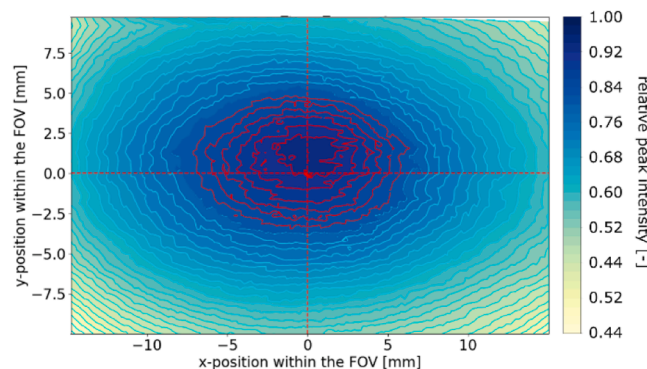


Fig. 22. Mapping of the laser beam relative peak Intensity measured within a 30 mm x 20 mm field of view centred around the centre of the lens objective. The dashed red lines represent the  $u$ - and  $v$ - optical axes and the centre of the lens objective. The solid red lines mark the levels within the relative peak intensity is 80% and above.

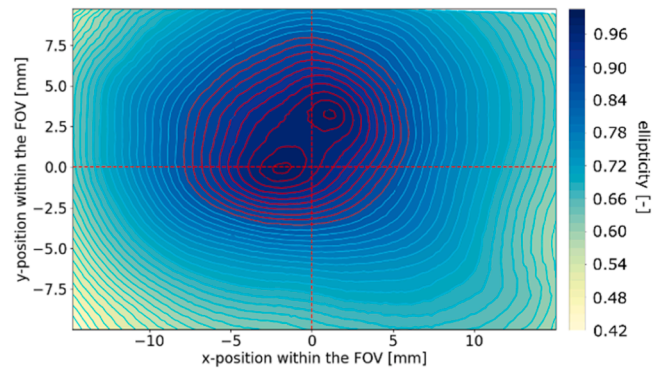


Fig. 23. Mapping of ellipticity  $\epsilon$  [-] measured within a 30 mm x 20 mm field of view centred around the centre of the lens objective. The dashed red lines represent the  $u$ - and  $v$ - optical axes and the centre of the lens objective. The solid red lines mark the levels within the ellipticity is 87% and above the beam can be considered circular.

circular in the centre of the lens objective with a beam diameter of ca.  $9.5 \mu\text{m}$  and becomes elliptical at the corners with approx.  $d_{\sigma m} = 11.5 \mu\text{m}$  and  $d_{\sigma M} = 25 \mu\text{m}$ . This corresponds to more than tripling the area of the laser spot.

With the different mappings, the beam properties of the laser tool can be described across the measured field of view. Together with the measurement of the positioning accuracy this is described as the tool fingerprint of the laser system. It is used to choose a suitable machining origin and scan area size. Furthermore, the tool fingerprint is used to investigate the influence of the different properties of the laser beam on the machining in terms of precision, removal rate and surface quality. Some tests on material removal rate and surface quality are conducted within this work and are presented in Section 4.6. The differences in laser shape and beam properties affect the outcome for processes such as marking, drilling, or ablation. Using the tool fingerprint of the laser system enables a better understanding, monitoring and prediction of laser processing within the calibrated and measured field of view.

#### 4.5. Temperature and time stability of the calibration

The positioning accuracy of the laser system after the calibration may change due to temperature changes of the system during experiments or production. For this purpose, the accuracy of the laser system is

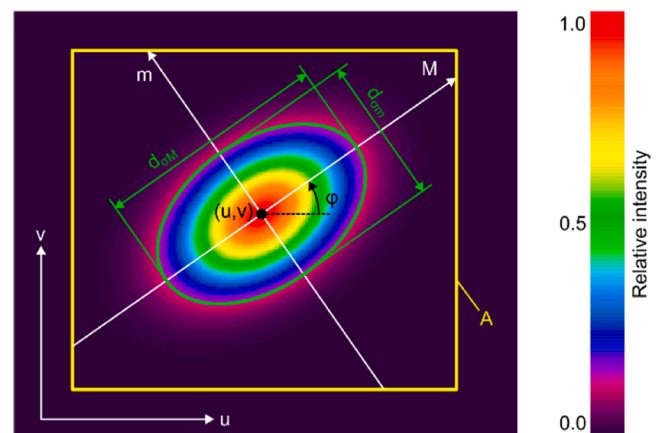


Fig. 24. Mapping of the measured intensity distribution of a rotated elliptical gaussian laser beam at the focal height. The coordinates of the beam centroid are  $(u, v)$ . The principal coordinate system of the rotated ellipse is  $M$  and  $m$ . Its origin is identical to the beam centroid. Only pixel inside the measurement aperture are used for the calculations. The calculated elliptical diameters  $d_{\sigma M}$  (major axis diameter) and  $d_{\sigma m}$  (minor axis diameter) are shown in green.



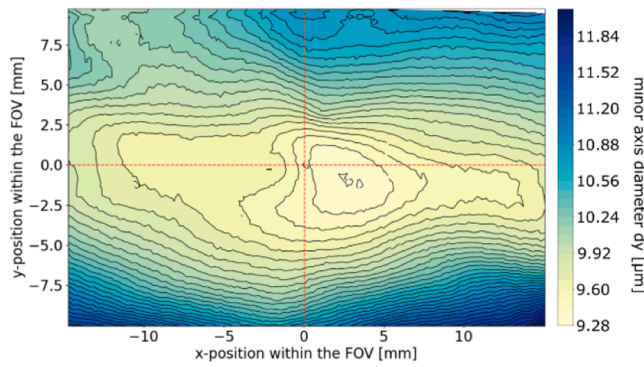


Fig. 25. Mapping of the minor axis diameter  $dy$  of the laser spot within a 30 mm x 20 mm field of view centred around the centre of the lens objective. The dashed red lines represent the u- and v- optical axes and the centre of the lens objective.

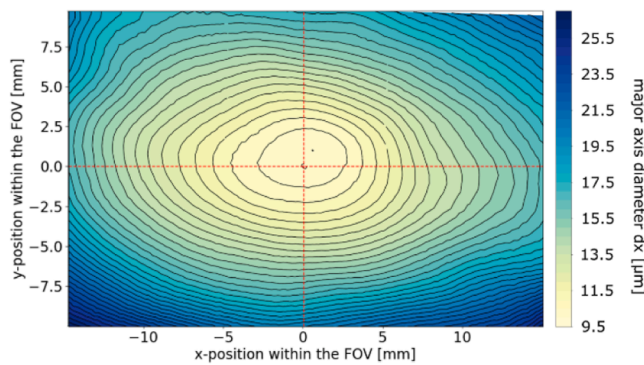


Fig. 26. Mapping of the major axis diameter  $dx$  of the laser spot within a 30 mm x 20 mm field of view centred around the centre of the lens objective. The dashed red lines represent the u- and v- optical axes and the centre of the lens objective.

measured over 240 min. Before the measurement, the laser is turned on at maximal power ( $P_{AVG} = 40$  W) into a beam dump to achieve stable conditions in terms of power and pointing stability. This is followed by a load cycle, that lasts for 15 min and mimics an experiment or a production of parts. Such a load cycle consists of alternating between turning on the laser at maximal power ( $P_{AVG} = 40$  W) for 30 s to heat up the mirrors and moving the galvo mirrors for 30 s in a sinusoidal motion. The sinusoidal oscillations ensures that there is always a driving force acting on the galvo mirrors and therefore electric current producing heat.

After 240 min, the maximal deviation error length measured lays within 1  $\mu$ m inside a circular field with a diameter of 30 mm, referenced to the measurement at the start ( $t = 0$  min), shown in Fig. 27. This proves that the calibration was stable during machining and did not change after multiple load cycles. Consequently, applying the self-optimizing calibration method proposed in this work with the hardware described in Section 2.1 ensures high laser manufacturing accuracy.

The accuracy of the laser system may also change over a period of days. Different reasons are responsible for this. Due to the assembly or disassembly of different experiments, the axes or mirrors may be displaced slightly and change the straightness of the beam path. It is also possible, that the laser beam exits from the laser device at a slightly different position after switching it off and on, or that the axes do not move exactly to the same position after switching them off and on. Therefore, the accuracy of the mechanical and optical axes is measured over a period of 39 days. They are measured separately on different days to reduce systematic errors. Furthermore, the system is used for various experiments and productions that do not allow regular measurements on

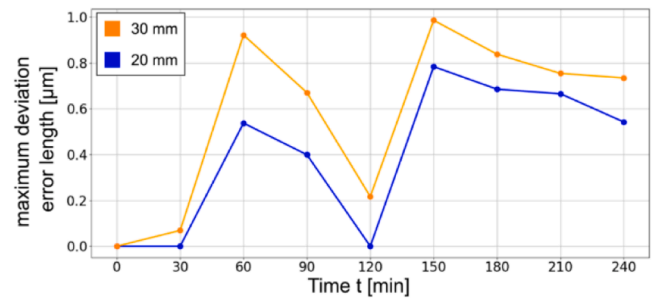


Fig. 27. Relative development of the maximal deviation error length during the thermal stability experiments for the optical u-v axes using the method of calibration phase 3.

fixed days and times but resemble real production in an industrial environment. As can be seen from Figs. 31 and 30, the high accuracy is lost after the laser system is turned off and switched on the following day. Within a smaller scan field, the deviations remain in a smaller range. Nevertheless, the maximal deviation error length ( $l_{e,uv}$ ) remains within a range of 18  $\mu$ m. This accuracy can be increased once again by one or few iterations of the automatic recalibration cycle of phase three presented in Section 4.3.

#### 4.6. Material removal and surface quality within the maximal markable scan field

The mapping of the properties of the laser beam within the field of view determined in Section 4.4 has shown that the properties of the laser change considerably at different radial positions. According to the data sheet, the lens objective is specified for the use of marking with it within a field of the size 15 mm x 15 mm (white dashed square shown in Fig. 29). The real maximal markable field is significantly bigger than that and has the shape of an ellipse that is cut off on the left and right side. To determine the influence of the different laser beam properties on the material removal and quality of the surface after machining, a grid of 1.3 mm x 1.3 mm squared pockets is machined on copper within the maximal markable field, shown in Fig. 29. A copper plate is used instead of the steel foil, because it is sufficiently thick (1.0 mm) and has an adequate surface quality and evenness. Identical pockets are machined, keeping the copper plate in the same place, and using only the optical axes to ablate the same pocket at different distances from the origin. The distance between the surface of the copper plate and the focal height within the field of view is measured before machining and adjusted to be in the range of  $\pm 8.0$   $\mu$ m, which is far smaller than the Rayleigh length of approx. 114.0  $\mu$ m.

Differences in the material removal at different positions within the FOV are visible in the microscopic image, shown in Fig. 29. As mentioned above, the totality of the ablated pockets again forms an ellipsis, which is cut off at the right and left sides. This is due to the physical limit of one of the galvo mirrors. At the edges, the pockets become brighter and appear silver at the outermost edge. This is due to the increased spot size and distorted shape of the spot (shown in Figs. 24 and 26). In addition to the microscopic image, the surface topography of the different pockets is measured with a confocal microscope at 20 x magnification, shown in the left image of Fig. 28. From the measurements it is found that the average depth of the ablated pockets varies at different positions up to 30%. The dependence of the ablation depth on the position within the scan field appears to be symmetrical. The lowest average removal depth is found in the edges of the field of view. In addition, the pockets in the centre and close to the top of the field of view have a low average removal depth. The highest average removal depth is found in the left and bottom of the field of view. The measured surface roughness (see Fig. 29 right image) is more uniform at the top, the middle and the bottom and increases towards the left and right side

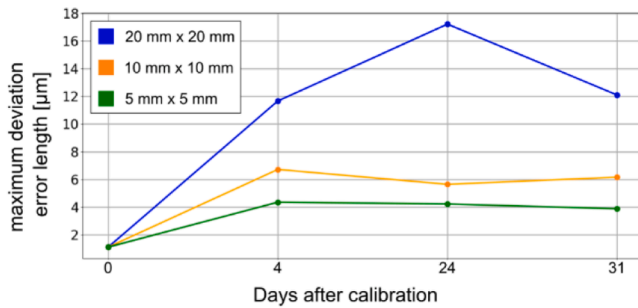


**Fig. 28.** Relative evolution of the maximal deviation error length of the optical axes within a measurement field of different during the long-term over a period of 31 days.

of the field of view. These measurements illustrate the importance of choosing the size and position of the marking field when increased homogeneity of ablation is required. They also show that the size of the scan field specified by the lens manufacturer can be extended considerably and that different characteristics of the laser beam, as in the lower left corner of the left image of Fig. 29, lead to a better ablation rate and surface quality. Here, the laser beam is larger than in the centre of the lens and more elliptical. It can be deduced from this that a larger spot size increases the removal efficiency, which is achieved at the origin of the lens objective by over- or under-focusing the surface during machining.

## 5. Conclusion and outlook

This work presents a self-optimising method and software for calibrating a laser system for micromachining. This allows us to compensate for the influence of errors on positioning accuracy that occur during the assembly of the laser machine itself and during the assembly and disassembly of fixtures for experiments or production. In addition, it is possible to compensate for the optical distortion of the objective lens and superimposed errors of other optical elements along the beam path. The measurements on which the calibration is based simultaneously confirm the accuracy achieved by the laser system. With the presented methodology a positioning accuracy in the micrometre range can be reached across the scan field that clearly exceeds the specified scan field size of the lens manufacturer and is temperature stable during machining. Furthermore, the developed software and method allows to maintain this accuracy through automatic monitoring and, if necessary, automatic recalibration of the laser system. However, it must be taken into account that complete automation of the recalibration is currently only possible for the optical axes and the maximum deviation error must be less than 0.2 mm.

The mapping of the tool fingerprint of the laser system, presented for the first time in this paper, provides an enhanced insight and

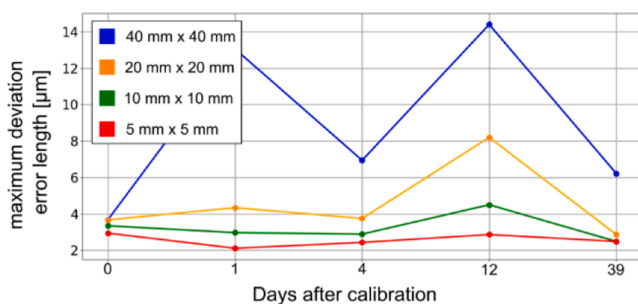


**Fig. 29.** Relative evolution of the maximal deviation error length of the optical axes within a measurement field of different size during the long-term over a period of 39 days.

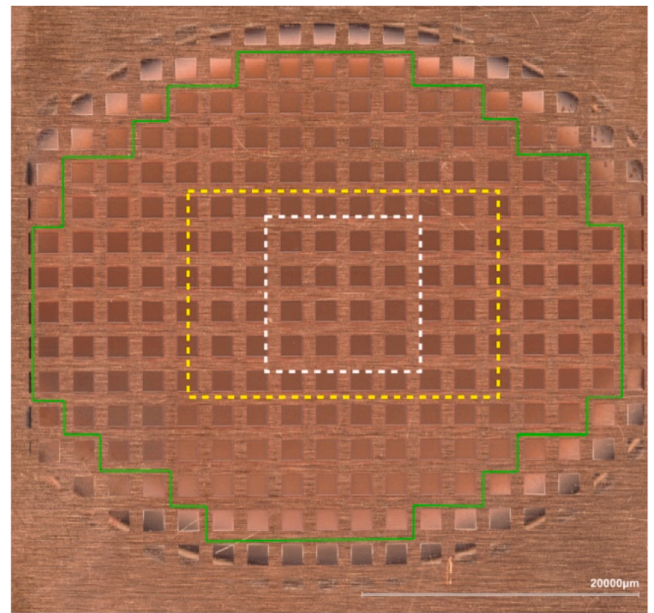


**Fig. 30.** Microscopic image of the laser machined copper plate to measure the removal rate and surface quality at different positions within the field of view. The yellow dashed rectangle represents the size of the area where the tool fingerprint was measured (30 mm x 20 mm). The white dashed square represents the size of the field of view specified in the datasheet of the lens objective used (15 mm x 15 mm). The green line represents the limit which all ablated pockets have been measured to investigate the surface quality.

understanding of laser processing in general and the calibrated laser system in particular. As a result, the machining strategy can be fine-tuned to optimise ablation efficiency and surface quality. Moreover, it is possible to select the size and position of the scan field to guarantee the desired homogeneity of processing. These findings are backed by the measurement of ablated pockets within the field of view on a copper plate.

The methods and algorithms presented here, and the introduction of the tool fingerprint represent an extension to the state of the art in order to better understand and improve laser processing and to increase the manufacturing accuracy and homogeneity of laser machining.

## CRediT authorship contribution statement

**M. Putzer:** Conceptualization, Methodology, Software, Validation, Investigation, Data curation, Visualization, Formal analysis, Writing – original draft, Writing – review & editing. **M. Zweifel:** Methodology, Software, Validation, Investigation, Data curation, Visualization, Formal analysis, Writing – original draft, Writing – review & editing. **F. Kneubühler:** Methodology, Validation, Investigation, Data curation, Writing – original draft, Writing – review & editing. **G. Rogério da Silva:** Validation, Investigation, Data curation, Visualization, Validation, Writing – review & editing. **K. Michael:** Investigation, Data curation, Writing – review & editing. **N. Schröder:** Validation, Data curation, Writing – review & editing. **T. Schudeleit:** Validation, Writing – review & editing, Supervision. **M. Bambach:** Writing – review & editing, Supervision, Project administration. **K. Wegener:** Writing – review & editing, Supervision, Project administration, Funding acquisition.

## Declaration of competing interest

The authors declare that they have no known competing financial interests or personal relationships that could have appeared to influence the work reported in this paper.



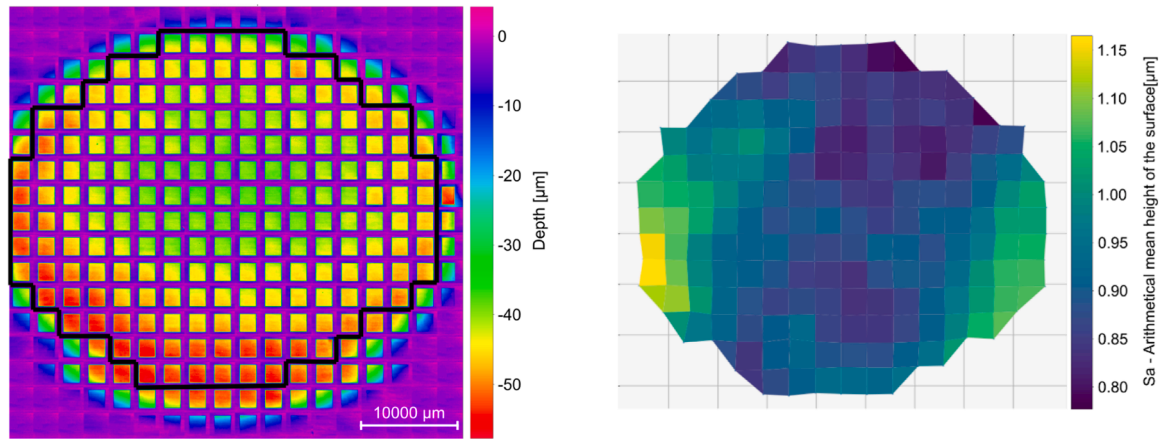


Fig. 31. left image: heat map of the topography of the surface after the laser machining. The lateral resolution was reduced to create the heat map. The pockets were measured by a confocal microscope at a magnification of 20 x. The black line is the size of the area where the surface quality was analyzed. Right image: heat map of the arithmetical mean height of the surface for the evaluation of the surface roughness.

### Data availability

Data will be made available on request.

### References

- [1] Noor MY, Tam MY, Lim LEN, Jana S. A review of the Nd: YAG laser marking of plastic and ceramic IC packages. *J Mater Process Technol* 1994;42(Issue 1):95–133. [https://doi.org/10.1016/0924-0136\(94\)90078-7](https://doi.org/10.1016/0924-0136(94)90078-7). Pages.
- [2] Velotti C, Astarita A, Leone C, Genna S, Minutolo FMC, Squillace A. Laser marking of titanium coating for aerospace applications. *Procedia CIRP* 2016;41:975–80. <https://doi.org/10.1016/j.procir.2016.01.006>. Pages.
- [3] Lasagni AF, Gachot C, Trinh KE, Hans M, Rosenkranz A, Roch T, Eckhardt S, Kunze T, Bieda M, Günther D, Lang V, Mücklich F. Direct laser interference patterning, 20 years of development: from the basics to industrial applications. *SPIE Proc* 2017;10092. <https://doi.org/10.1117/12.2252595>.
- [4] Brannon JH, Tam AC, Kurth RH. Pulsed laser stripping of polyurethane-coated wires: a comparison of KrF and CO<sub>2</sub> lasers. *J Appl Phys* 1991;70:3881–6. <https://doi.org/10.1063/1.349195>.
- [5] Neuschwander B. *Laser micromachining in: handbook of laser technology and applications, III. CRC Press Taylor and Francis Group; 2021. p. 47–69. Page.*
- [6] Warhanek M, Walter C, Hirschi M, Boos J, Bucourt WK. Comparative analysis of tangentially laser-processed fluted polycrystalline diamond drilling tools. *J Manuf Process* 2016;23:157–64. <https://doi.org/10.1016/j.jmapro.2016.06.023>. Pages.
- [7] Warhanek M, Pfaff J, Martin P, Schönbacher BJ, Wegener K. Geometry optimization of polycrystalline diamond tools for the milling of sintered ZrO<sub>2</sub>. *Procedia CIRP* 2016;46:290–3. <https://doi.org/10.1016/j.procir.2016.04.003>. Pages.
- [8] Antar M, Chantzis D, Marimuthu S, Hayward P. High speed EDM and laser drilling of aerospace alloys. *Procedia CIRP* 2016;42:526–31. <https://doi.org/10.1016/j.procir.2016.02.245>. Pages.
- [9] Wu L, Wang L, Wang S, Xiao T, Chen M, Shao Q, York P, Singh V, Yin X, Gu J, Zhang J. Three dimensional structural insight of laser drilled orifices in osmotic pump tablets. *Eur J Pharmaceut Sci* 2016;93:287–94. <https://doi.org/10.1016/j.ejps.2016.08.039>. Pages.
- [10] Wang XC, Zheng HY. High quality laser cutting of electronic printed circuit board substrates. *Circ World* 2009;35:46–55. <https://doi.org/10.1108/03056120911002415>. Pages.
- [11] Thibault F. (2018) High repetition rate USP lasers improve OLED cutting results, Coherent White Paper, [https://content.coherent.com/legacy-assets/pdf/COHR\\_WhitePaper\\_High\\_Repetition\\_Rate\\_USP\\_Lasers\\_Improve\\_OLED\\_Cutting\\_Results.pdf](https://content.coherent.com/legacy-assets/pdf/COHR_WhitePaper_High_Repetition_Rate_USP_Lasers_Improve_OLED_Cutting_Results.pdf) [accessed 25 March 2024].
- [12] Ahn S, Kim J, Lee D, Park C, Zander C, Ji SY, Chang WS. Enhancement of electrical conductivity during the femtosecond laser trimming process for OLED repair. *Opt Lasers Eng* 2021;137. <https://doi.org/10.1016/j.optlaseng.2020.106381>. Vol.
- [13] Product Brochures for CALsheet from Scanlab GmbH, 06 /2019, <https://www.scanlab.de/sites/default/files/2020-08/CalibrationSolutions.pdf> [accessed 25 March 2024].
- [14] Xie J, Huang S, Duan Z, Shi Y, Wen. Correction of the image distortion for laser galvanometric scanning system. *Opt Laser Technol* 2005;37:305–11. <https://doi.org/10.1016/j.optlastec.2004.04.012>. Pages.
- [15] Zhang T, Liang Y, Wang H, Wu C, Zhang G, Huang Y, Rong Y. Field distortion correction in galvanometric scanning system by interpolation with symmetric polynomials. *Precis Eng* 2023;83:134–41. <https://doi.org/10.1016/j.precisioneng.2023.06.001>. Pages.
- [16] Zhimuleva ES, Zavyalov PS, Kravchenko MS. Development of telecentric objectives for dimensional inspection systems. *Optoelectronics, Instrum Data Process* 2016;54:52–60. <https://doi.org/10.3103/S8756699018010090>. Pages.
- [17] Manakov A, Seidel HP, Ihrke I. A mathematical model and calibration procedure for galvanometric laser scanning systems. *Vision Model Vis* 2011. <https://doi.org/10.2312/PE/VMV/VMV11/207-214>.
- [18] Godineau K, Lavernhe S, Tournier C. Calibration of galvanometric scan heads for additive manufacturing with machine assembly defects consideration. *Addit Manuf* 2019;26:250–7. <https://doi.org/10.1016/j.addma.2019.02.003>. Pages.
- [19] Delgado MAO, Lasagni AF. Reducing field distortion for galvanometer scanning system using a vision system. *Opt Lasers Eng* 2016;86:106–14. <https://doi.org/10.1016/j.optlaseng.2016.05.016>. Pages.
- [20] Chen X, Li C, Wang Y, Yuan K. An algorithm for correction of distortion of laser marking systems. In: 2007 IEEE International Conference on Control and Automation; 2007. p. 487–91. <https://doi.org/10.1109/ICCA.2007.4376404>. Pages.
- [21] Chen MF, Chen YP, Hsiao WT. Correction of field distortion of laser marking systems using surface compensation function. *Opt Lasers Eng* 2009;47:84–9. <https://doi.org/10.1016/j.optlaseng.2008.07.017>. Vol.Pages.
- [22] Bessmeltsev VP, Goloshevsky NV, Kasterov VV, Kipriyanov Ya A, Smirnov KK. Method of calibration of a laser-based galvanometric scanning system with submicron resolution. *Optoelectronics, Instrum Data Process* 2018;54:390–6. <https://doi.org/10.3103/S8756699018040118>. Pages.
- [23] Chen G, Zhang Y, Tian P. An error compensation method based on machine vision for laser-processing systems with galvanometers. *Appl Phys B* 2021;127. <https://doi.org/10.1007/s00340-020-07550-0>. Vol.article number 3.
- [24] Grzhibovskis R, Bambach M, Rjasanow S, Hirt G. Adaptive cross-approximation for surface reconstruction using radial basis functions. *J Eng Math* 2007;62:149–60. <https://doi.org/10.1007/s10665-007-9197-8>. Pages.
- [25] Green J. Locating tie-points on a grid. *Nasa Tech Rep Server* 1993:19940023403. <https://ntrs.nasa.gov/citations/19940023403>.
- [26] Z. Marc, M. Putzer (2023) Intersection-finder, <https://github.com/MarcZweifel/Intersection-finder> [accessed 25 March 2024].
- [27] Z. Marc, M. Putzer (2023) BeamGage-automation, <https://github.com/MarcZweifel/BeamGage-automation> [accessed 25 March 2024].
- [28] Lasers and laser-related equipment - Test methods for laser beam widths, divergence angles and beam propagation ratios - Part 1: stigmatic and simple astigmatic beams (ISO 11146-1:2021); German version EN ISO 11146-1:2021, [doi:10.31030/3258715](https://doi.org/10.31030/3258715).